Volume 19 Issue 8
Originally issued as D1

Global Journal of Medical Research: D
Adiology, Diagnostic and Instrumentation
Volume 19 Issue 1 Version 1.0 Year 2019
Type: Double Blind Peer Reviewed International Research Journal
Publisher: Global Journals
Online ISSN: 2249-4618 & Print ISSN: 0975-5888

Application of Eshelby's Solution to Elastography for Diagnosis of Breast Cancer

By Bonghun Shin, Darindra Gopaul, Samantha Fienberg & Hyock Ju Kwon
University of Waterloo

Abstract- Eshelby's solution is the analytical method that can derive the elastic field within and around an ellipsoidal inclusion embedded in a matrix. Since breast tumor can be regarded as an elastic inclusion with different elastic properties from those of surrounding matrix when the deformation is small, we applied Eshelby's solution to predict the stress and strain fields in the breast containing a suspicious lesion. The results were used to investigate the effectiveness of strain ratio (SR) from elastography in representing modulus ratio (MR) that may be the meaningful indicator of the malignancy of the lesion. This study showed that SR significantly underestimates MR and is varied with the shape and the modulus of the lesion. Based on the results from Eshelby's solution and finite element analysis (FEA), we proposed a surface regression model as a polynomial function that can predict the MR of the lesion to the matrix. The model has been applied to gelatin-based phantoms and clinical ultrasound images of human breasts containing different types of lesions. The results suggest the potential of the proposed method to improve the diagnostic performance of breast cancer using elastography.

Keywords: *eshelby's solution, elastography, breast cancer, mechanical properties, strain ratio, modulus ratio.*

GJMR-D Classification: *NLMC Code: WB 200*

APPLICATIONOFESHELBYSSOLUTIONTOELASTOGRAPHYFORDIAGNOSISOFBREASTCANCER

Strictly as per the compliance and regulations of:

Open Association of Research Society, USA
Research | Diversity | Ethics

© 2019. Bonghun Shin, Darindra Gopaul, Samantha Fienberg & Hyock Ju Kwon. This is a research/review paper, distributed under the terms of the Creative Commons Attribution-Noncommercial 3.0 Unported License http://creativecommons.org/licenses/by-nc/3.0/), permitting all non-commercial use, distribution, and reproduction in any medium, provided the original work is properly cited.

Application of Eshelby's Solution to Elastography for Diagnosis of Breast Cancer

Bonghun Shin [α], Darindra Gopaul [σ], Samantha Fienberg [ρ] & Hyock Ju Kwon [ω]

Abstract- Eshelby's solution is the analytical method that can derive the elastic field within and around an ellipsoidal inclusion embedded in a matrix. Since breast tumor can be regarded as an elastic inclusion with different elastic properties from those of surrounding matrix when the deformation is small, we applied Eshelby's solution to predict the stress and strain fields in the breast containing a suspicious lesion. The results were used to investigate the effectiveness of strain ratio (SR) from elastography in representing modulus ratio (MR) that may be the meaningful indicator of the malignancy of the lesion. This study showed that SR significantly underestimates MR and is varied with the shape and the modulus of the lesion. Based on the results from Eshelby's solution and finite element analysis (FEA), we proposed a surface regression model as a polynomial function that can predict the MR of the lesion to the matrix. The model has been applied to gelatin-based phantoms and clinical ultrasound images of human breasts containing different types of lesions. The results suggest the potential of the proposed method to improve the diagnostic performance of breast cancer using elastography.

Keywords: eshelby's solution, elastography, breast cancer, mechanical properties, strain ratio, modulus ratio.

I. Introduction

Recently, breast elastography has emerged as a new screening modality for breast cancers.[1-3] Elastography uses palpation principle to detect and classify pathological lesions using elastic properties of tissues.[4] Because pathological lesions are normally stiffer than benign tissues, the strain in the lesion is less than the surrounding tissue under compression.[5] Strains are calculated using the time-gradient of radiofrequency (RF) echo signals[6] or displacement-gradient of B-mode images,[7] obtained before and after a slight compression of the tissue. Resulting strains are displayed as a color-coded image, called elastogram as a map of tissue elasticity.

Elastography can be further classified into strain (or quasi-static) elastography[6] and shear wave (or transient) elastography, [8, 9] according to tissue compression method. In strain elastography, tissue is deformed by applying slight axial compression using a conventional transducer, or alternatively deformation can be produced by respiratory movements. The profile of tissue deformation is converted to a strain map from which elastogram is derived.[6] In shear wave elastography, elastograms are obtained based on the combination of a radiation force induced in a tissue by an ultrasonic beam and an ultrafast imaging sequence capable of catching in real time the propagation of the resulting shear waves.[8, 9] The local shear wave velocity is recovered, enabling the production of a two-dimensional map of shear elasticity.[10]

There have been various efforts to utilize elastography for the diagnosis of breast cancer. It oh et al.[11] proposed a five-point elasticity scoring system on the basis of overall pattern, similar to BIRADS (Breast Imaging Reporting and Data System) criteria[2] for ultrasound (US) and mammogram. It is also known that the size of the tumor determined by elastogram is significantly larger than that in sonogram, only when the tumors are carcinomas.[6] However, most commonly accepted diagnostic measure is strain ratio (SR), [6, 12, 13] which is the ratio of the compressive strain in surrounding tissue to that of a suspicious lesion (also called "observed con- trast"[14] or "strain contrast"[15]). Thomas et al. performed a clinical study to evaluate the performance of SR in differentiating benign and malignant breast lesions.[12] They reported that SR cutoff value of 2.45 allowed significant differentiation ($p < 0.001$) of malignant (5.1 ± 4.2) and benign (1.6 ± 1.0) lesions. Zhi et al. conducted a similar study to compare the diagnostic performance of SR with that of five-point elasticity scoring system.[13] They concluded that SR-based elastography could provide a more reliable diagnostic tool, and the cutoff SR of 3.05 resulted in significant differentiation ($p < 0.00001$) between malignant (8.38 ± 7.65) and benign (1.83 ± 1.22) lesions.

The use of SR as a diagnostic measure is based on the assumption that SR is directly related to modulus ratio (MR: the ratio of the elastic moduli of the inclusion and of the surrounding tissue; also called "true contrast"[14] or "modulus contrast"[15]), which is considered as a true indicator of the malignancy of lesion. However, only a handful of studies are found in the literature that mechanically measured the elastic moduli of breast tissues. Most frequently referred one was conducted by Krouskop et al.[16] which reported that elastic modulus of invasive carcinoma was 5 and 25 times higher than that of normal tissue at the compression levels of 5% and

Author α ω: Department of Mechanical and Mechatronics Engineering, University of Waterloo, 200 University Ave. W., Waterloo, Ontario, Canada N2L 3G1. e-mail: hjkwon@uwaterloo.ca
Author σ: Radiation Oncology, Grand River Regional Cancer Centre, Kitchener, Ontario, Canada.
Author ρ: Radiology, Grand River Hospital, Kitchener, Ontario, Canada.

© 2019 Global Journals

20%, respectively. Sarvazyan et al.[17] also reported that fibroadenomas are typically four times stiffer than normal tissue, whereas cancers can be as much as seven times stiffer. More recently, Samani et al.[18] measured the elasticity of breast normal tissues and tumors and reported that breast cancers exhibited 6 to 13 fold increased stiffness compared with normal tissue.

There also have been attempts to infer MR from the measured SR, using either a simplified or continuum mechanical model, via inverse reconstruction schemes. Raghavan and Yagle[19] proposed a direct inversion scheme for recovering shear modulus by deriving a linear system of elasticity equations for the plane–strain condition. The weakness of their approach is that hydrostatic pressure on the boundary must be known to solve the equations. Skovoroda et al.[20] used an analytical method to eliminate the pressure term from the equations. Later on, Skovoroda et al.[5] regarded the inverse problem as an integral rather than a differential form to make the technique less susceptible to measurement noise. Sumi et al.[21, 22] proposed a direct inversion scheme by solving the inverse problem for the plane–stress case, and Le Floc'h et al. [23] extended the concept to the plane–strain case. Barbone and Oberai [24] derived the reconstruction formulae for some special elastic inverse problems, including 2D and 3D, and compressible and incompressible materials. There also have been attempts to view the inverse problem as a parameter optimization problem, where the goal is to find the shear modulus that minimizes the error between measured strain field and those computed by solving the direct problem.[25] For this iterative inversion approach, Hessian-based optimization method, [26-28] gradient-based optimization method, [25,29] and gradient-free optimization method [30-32] were used.

As one of the efforts to relate MR and SR, Kallel et al.[14] used a classical analytic solution of the elasticity equations for an infinite medium subjected to a uniaxial compression to derive a closed form relationship between SR and MR. For incompressible materials ($\nu = 0.5$), they derived the following relationship:

$$MR = 2\,SR - 1. \tag{1}$$

Biligen and Insana[33] also derived an approximate expression for extremely hard inclusion and incompressible materials:

$$MR = 2.5\,SR. \tag{2}$$

Note that the above derivations are limited to 2D with simple inclusion shapes such as sphere or cylinder, although malignant tumors are known to have irregular or ellipsoidal shapes.[34] Therefore, it is essential to derive more general solutions that can relate SR and MR for 3D shapes of inclusions.

Finite element models were also used to estimate the elastic behavior in various types of lesions and surrounding tissues. Kallel et al.[14] investigated the effect of lesion boundary conditions, depth, and modulus contrast on axial strain field by finite element analysis (FEA), assuming planestrain condition and linear elastic materials. Biligen and Insana[33] performed the FEA on an axisymmetric model with a spherical inclusion and concluded that the size of the compressor, location of an inclusion relative to the compressor, and type of compression (uniform stress vs. uniform displacement) alter the strain and stress distributions. Recently, Celi et al.[15] performed the FEA study using simple axisymmetric and more realistic anthropomorphic models. They concluded that simple axisymmetric model has many similarities with the anthropomorphic one and is suitable for elastosonography simulations.

From the point of solid mechanics, breast tumor can be regarded as an elastic inclusion that has different elastic properties from those of the surrounding matrix. Although human tissues show highly nonlinear stress–strain behavior,[35] they can be regarded as linear elastic in the small strain region.[7] In particular, the practice for elastography applies only a small amount of axial compression (typically on the order of 2% strain[36]) to avoid decorrelation errors[4]; therefore, the assumptions of linear elastic inclusion and matrix are reasonable. Based on linear elasticity, Eshelby[37] derived the elastic field inside the elliptic inclusion using the biharmonic potential and Green's tensor. His solution yielded a surprising result that the stress (and strain) within an ellipsoidal inclusion embedded within a matrix subjected to a remote load is homogeneous. In the subsequent paper, 38 he derived that the elastic field outside an ellipsoidal inclusion is given in a form that involves only the harmonic potential of an ellipsoid and can be reduced to a form suitable for numerical calculation of the stress.

We applied Eshelby's solution to the elastic medium containing an ellipsoidal inclusion to determine the elastic fields within and outside the inclusion. Although similar analyses can be pursued by FEA, Eshelby's solution requires much less time and effort than FEA, once the method is established. Also, in general, well-posed analytical approach can yield exact solutions without the issues of meshing effect and/or convergence problem, compared with the approximate solutions from numerical approaches. Compared to inverse methods, Eshelby's solution is much less susceptible to measurement noises and mathematically simpler, and hence requires much less computation. However, current solution is still limited to relatively simple 3D shapes (spheroids).

The results from Eshelby's solution were verified with FEA simulations using axisymmetric models. Based on the results, the relationship between SR and the shape of the inclusion and MR was derived as a simple analytical relationship by using a surface regression

© 2019 Global Journals

model, and the relationship was verified using gelatin-based phantoms. The model was further applied to the elastograms of human breasts with different types of lesions, and the results were statistically analyzed to compare the performance of SR and MR in breast cancer screening. This paper concludes that the proposed method adopting MR as an indicator has the potential to better diagnose the malignant tumor than the conventional SR.

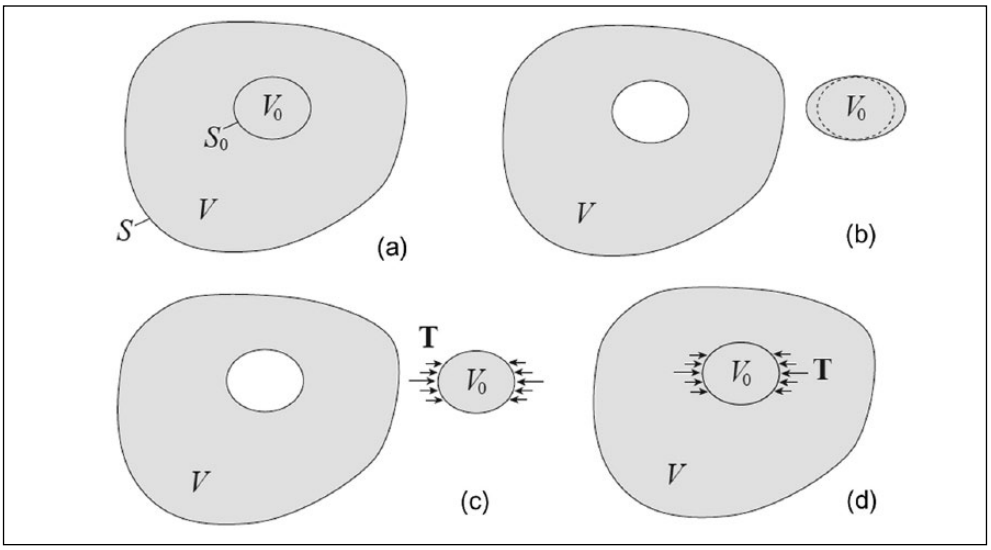


Figure 1: Four steps of a virtual experiment to construct Eshelby's solution: (a) a linear elastic solid with volume *V* and surface *S* (matrix). An inclusion *V0* with surface *S0* is embedded into the matrix; (b) remove the inclusion from the matrix; (c) apply surface traction T to *S0* to make the inclusion return to its original shape; (d) put the inclusion back to the matrix and remove the traction T.

a) Eshelby's Solution

Eshelby[37,38] proposed a general method to derive the local strain and stress fields which can be induced by remote loading applied to an elastic infinite matrix V_0 (phase 0) containing an ellipsoidal inhomogeneous inclusion V_1 (phase 1; Figure 1a). Remote loading implies that stress is uniformly distributed over the matrix without causing local distortions or strain concentrations. He solved this problem elegantly by the superposition principle and the Green's function, through the four steps of a virtual experiment:

- *Step 1:* Remove the inclusion from the matrix (Figure 1b). Then the inclusion is strained due to loss of constraint from the matrix (eigenstrain ε^{**}).
- *Step 2:* Apply the surface traction T to S_0 in order to make the inclusion return to its original shape (Figure 1c). The elastic strain of the inclusion should exactly cancel the eigenstrain.
- *Step 3:* Put the inclusion back to the matrix. The same force *T* is applied to the inclusion surface S_0 (Figure 1d). There is no change in the strain fields in either the inclusion or the matrix from Step 2.
- *Step 4:* Now remove the traction *T*. This makes the problem return the original inclusion problem in Figure 1(a). The change from Step 3 to Step 4 is equivalent to applying a can- celing body force F = −T to the inclusion surface S_0 of the elastic body.

Steps 1 to 4 can be mathematically derived in terms of the Green's function of the elastic body. The strain and stress inside the inclusion can be expressed as:

$$\boldsymbol{\varepsilon} = \boldsymbol{\varepsilon}^0 + \mathbf{S} : \boldsymbol{\varepsilon}^{**}, \tag{3}$$

$$\boldsymbol{\sigma} = \boldsymbol{\sigma}^0 + \mathbf{C}^0 \cdot [\mathbf{S} - \mathbf{I}] : \boldsymbol{\varepsilon}^{**}, \tag{4}$$

where $\boldsymbol{\varepsilon}^0$ is the remote strain, $\boldsymbol{\varepsilon}^{**}$ the eigenstrain, $\boldsymbol{\sigma}^0$ the remote stress, C^0 the stiffness tensor of the matrix, and I the identity tensor.[39] If the entire medium is loaded by the specified remote stress tensor $\boldsymbol{\sigma}^0$, then the corresponding strain $\boldsymbol{\varepsilon}^0$ is derived by Hooke's law:

$$\boldsymbol{\sigma}^0 = \mathbf{C}^0 : \boldsymbol{\varepsilon}^0. \tag{5}$$

Eshelby S tensor is a function solely of the ellipsoid dimensions and the Poisson's ratio of the matrix.[40] Explicit expressions for the components of S for various shapes of ellipsoid have been given by Mura,[40] and in more general form by Ju and Sun.[39,41] In Equations (3) and (4), the eigenstrain $\boldsymbol{\varepsilon}^{**}$ can be derived as:

$$\boldsymbol{\varepsilon}^{**} = (\mathbf{S} + \mathbf{A})^{-1} : (\mathbf{B} : \boldsymbol{\varepsilon}^t - \boldsymbol{\varepsilon}^0), \tag{6}$$

where $\boldsymbol{\varepsilon}^t$ is the prescribed eigenstrain, and the fourth-order mismatch tensors A and B are defined as:

$$\mathbf{A} = \left[\mathbf{C}^1 - \mathbf{C}^0\right]^{-1} \cdot \mathbf{C}^0, \ \mathbf{B} = \left[\mathbf{C}^1 - \mathbf{C}^0\right]^{-1} \cdot \mathbf{C}^1. \tag{7}$$

© 2019 Global Journals

For the external field, that is, points outside of the inclusion, stress and strain varies with position as follows:

$$\boldsymbol{\varepsilon}(\mathbf{x}) = \boldsymbol{\varepsilon}^{\mathbf{0}} + \overline{\mathbf{G}}(\mathbf{x}) : \boldsymbol{\varepsilon}^{**}, \quad \mathbf{x} \in V^0, \tag{8}$$

$$\boldsymbol{\sigma}(\mathbf{x}) = \boldsymbol{\sigma}^{\mathbf{0}} + \mathbf{C}^{\mathbf{0}} \cdot \overline{\mathbf{G}}(\mathbf{x}) : \boldsymbol{\varepsilon}^{**}, \quad \mathbf{x} \in V^0, \tag{9}$$

where x is a position vector, G(x) another fourth-order tensor which is a function of the ellipsoid geometry, Poisson's ratio of the matrix and the coordinate position.[38,40] The explicit expressions for all components of G(x) are provided by Ju and Sun.[39,41]

These mathematical solutions were coded into MATLAB functions (see the appendix) to calculate the elastic fields inside the inclusion and in the matrix. Key inputs of the code are elastic modulus *E*, Poisson's ratio ν, remote stress $\boldsymbol{\sigma}^0$, and the size of the inclusion. Prescribed eigenstrain $\boldsymbol{\varepsilon}^t$ is also an input, but merely 0 for the current applications. From those inputs, the code calculates eigenstrain $\boldsymbol{\varepsilon}^{**}$, Eshelby tensor S to finally produce the strain $\boldsymbol{\varepsilon}(x)$ and stress $\boldsymbol{\sigma}(x)$ fields, in the matrix and inclusion, respectively, as key outputs.

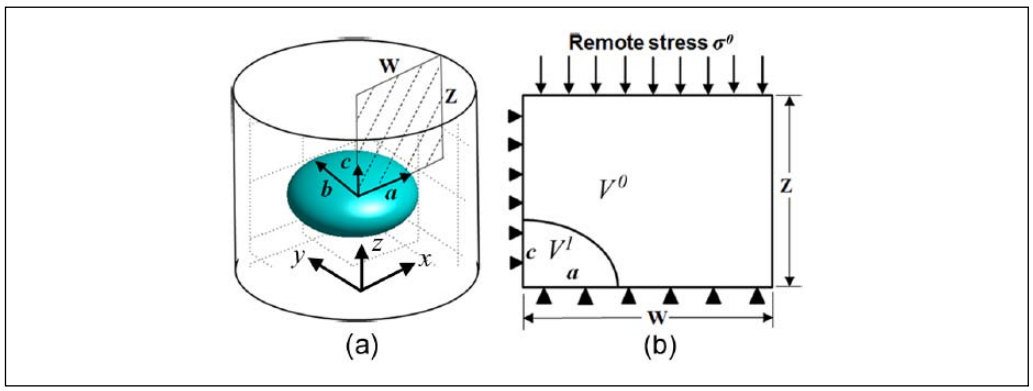


Figure 2: (a) Geometry of an ellipsoidal inclusion embedded in a matrix and (b) an axisymmetric FEA model (dotted area in (a)). Remote stress $\boldsymbol{\sigma}^0$ is applied to the top, and left and bottom edges are constrained in the *x*- and *z*-directions, respectively. In (a), position of coordinate system is arbitrary. FEA = finite element analysis.

II. Materials and Method

a) FEA Simulation

FEA simulations were performed to verify the results from Eshelby's solution using a commercial FEA code (Abaqus 6.10). Assuming inclusions in spheroidal shapes (ellipsoid of revolution), simulations were performed using axisymmetric models as depicted in Figure 2. Note that for axisymmetric models, axisymmetric FEA simulation is identical to 3D FEA.

The size and shape of the spheroidal inclusion is defined by the axes *a, b*, and *c* in *x*-, *y*-, and *z*-directions, respectively, as shown in Figure 2(a). The shape of the matrix is described by a cylindrical volume with height 2*Z* and diameter 2*W*. The matrix and inclusion are each homogeneous with isotropic elastic properties that are described by the elastic modulus E^0 and E^1, and Poisson's ratio ν^0 and ν^1, respectively. The interface between matrix and inclusion is assumed to be perfectly bonded. An 8-node quadratic axisymmetric quadrilateral element with reduced integration (CAX8R in Abaqus 6.10) was used, and the linear elastic deformation was assumed. In the elastography simulation, a static compressive force (remote stress $\boldsymbol{\sigma}^0$ in Figure 2b) was applied to the top surface of the cylinder, while left and bottom edges are constrained in the x- and z-directions, respectively.

b) Displacement-Gradient Elastography (DGE)

Digital image cross-correlation method was applied to B-mode US images to determine the displacement field developed by the compression.[42] To suppress the decorrelation errors in large deformation, dynamic referencing scheme[43,44] was used. Strains were calculated using displace- ment gradients as:

$$\varepsilon_x = \frac{\partial u_x}{\partial x}, \qquad \varepsilon_y = \frac{\partial u_y}{\partial y}, \tag{10}$$

and the roughness of strain field was reduced by applying smoothing algorithm.[45] Graphical representation of the resulting strain map is called DGE elastogram.

c) Gelatin Phantoms

Gelatin-based phantoms were designed to contain an inclusion with higher stiffness than the surrounding matrix, mimicking a carcinoma in a normal breast tissue.[46] Inclusions and matrixes were made with the same constituents to have the similar echogenicity, that is, 1 wt% agarose (J.T. Baker), 2 wt% glutaraldehyde (Sigma-Aldrich), 5 wt% n-propanol (Fisher-Scientific), gela- tin (Fluka; 20 wt% for inclusion and 5 wt% for matrices), and distilled water (the remaining wt%). The procedure to fabricate the phantoms is illustrated in Figure 3.[42]

© 2019 Global Journals

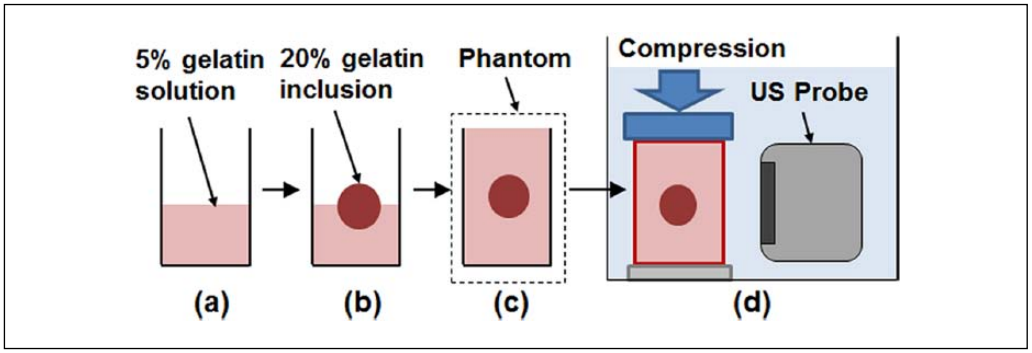


Figure 3: Schematics of phantom fabrication procedure and US imaging setup: (a) 5% gelatin solution was poured into the mold in half; (b) the solid inclusion containing 20% gelatin was placed on the solution; (c) gelatin solution was poured to fill the rest of the mold, and the mold was kept at room temperature for 48 hr for gelation; (d) for US imaging, the phantom was compressed while the US probe acquired US images. US = ultrasound.

Fabricated gelatin phantoms were US imaged using a commercial US scanner (Accuvix XQ, Medison, South Korea), while it was being compressed up to 10% strain at the loading rate of 100 μm/s. During compression, US images were taken with the US probe (L6-12IS, 6-12MHz) placed in the direction perpendicular to the axis of cylindrical inclusion (Figure 3d).

Stress–strain relationships of gelatin inclusion and matrix were determined by conducting separate compression tests on cylindrical samples with aspect ratio of 1 (height and diameter 4 cm each) that were additionally made at each formula. Each sample was loaded up to the engineering strain of 10% at 100 μm/s loading rate using TA material testing machine (Stable Micro Systems, England) with a 50 N load cell.

d) Clinical Applications

Small-scale clinical study was performed on 45 volunteer patients with different BIRADS lesions in their breasts. Patients underwent breast US imaging with Philips IU22 XMTRAIX US system in the Grand River Hospital (Kitchener, Ontario, Canada). US images were taken by a US technologist by applying a slight compression to the breast with a US probe (L17-5). DGE elastograms were produced by applying DGE method to US images. After imaging, all of the lesions were examined histologically with biopsy, but results had been kept until the end of analyses for nonbiased assessment.

III. Results and Discussion

a) Spherical Inclusion

Eshelby's solution was applied to a numerical phantom where a spherical inclusion (E^1 = 50 kPa) was embedded in the matrix (E^0 = 10 kPa) (MR = 5) and remote stress (σ^0 = 1 kPa) was applied in z (axial) direction. Remote strain in the matrix was 0.1 ($\varepsilon^0 = \sigma^0/E^0$). Poisson's ratios of both inclusion and matrix were assumed to be 0.45. Figure 4(a) and (b) show the 3D plots of axial stress (σ_z) and strain (ε_z) fields, and Figure 4(c) and (d) present axial stress and strain distributions in the x–z quarter-plane, respectively. As predicted by Eshelby,[4] stress and strain within the inclusion are uniform at 1.605 kPa and 0.0366, respectively. However, stress and strain varies significantly across the matrix. Highly concentrated stress and strain zones are formed right above the inclusion in the axial (z) direction, whereas significantly low stress and strain are observed right beside the inclusion in the lateral (x) direction. In the matrix far from the inclusion, stress field can be divided into two regions by the borderline inclined at about 45° (Figure 4c). Above the line, the stress is higher (1010~1250 Pa) than the applied stress, while lower (940~995 Pa) below the line. Meanwhile, strain field in the matrix (Figure 4d) can be divided into three regions: upper region with the strain higher than the remote strain (0.13~0.11), upper-right region with lower strain (0.092~0.099), and lateral region with the strain almost the same as the remote strain (0.1~0.103).

The effects of MR on strain fields were investigated by varying the modulus of spherical inclusion. Figure 5(a) and (b) show the strain field of phantoms containing an inclusion with MR = 2 and MR = 10 at 0.1 remote strain, respectively. Strain inside the inclusion decreases with the increase of MR (0.0696 at MR = 2; 0.0204 at MR = 10); however, far-field strain distribution in the matrix is not affected much by the change of MR. Particularly, the shape and the strain levels in the lateral regions are almost identical regardless of the change in inclusion modulus.

© 2019 Global Journals

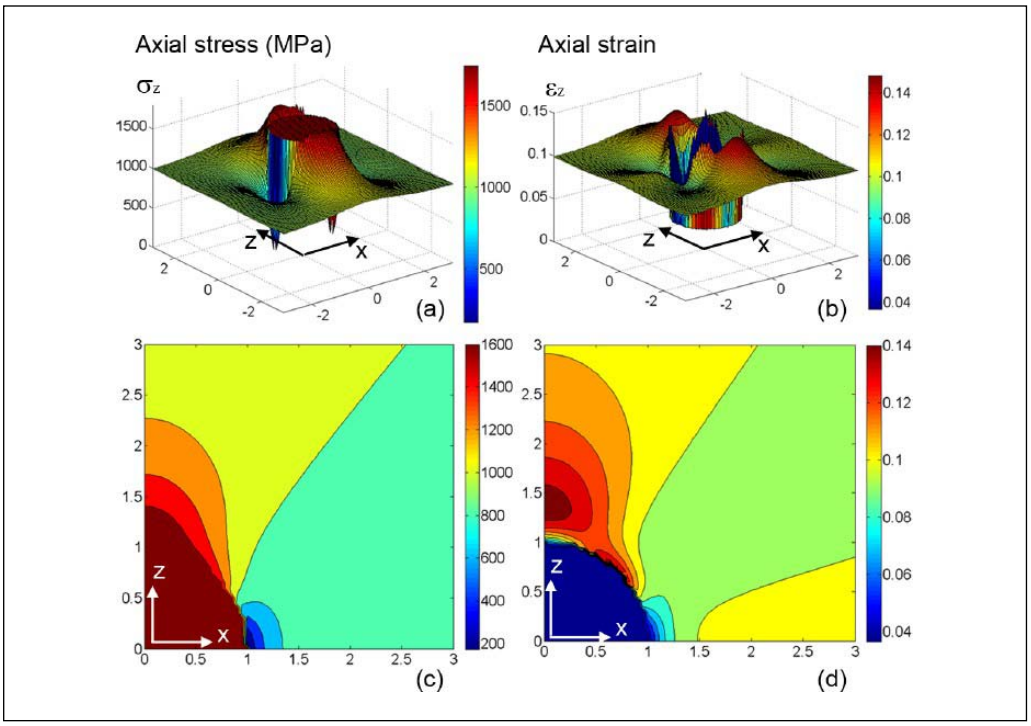


Figure 4: Axial stress and axial strain fields in the numerical phantom containing a spherical inclusion determined by Eshelby solution: (a) 3D axial stress, (b) 3D axial strain, (c) 2D axial stress, (d) 2D axial strain.

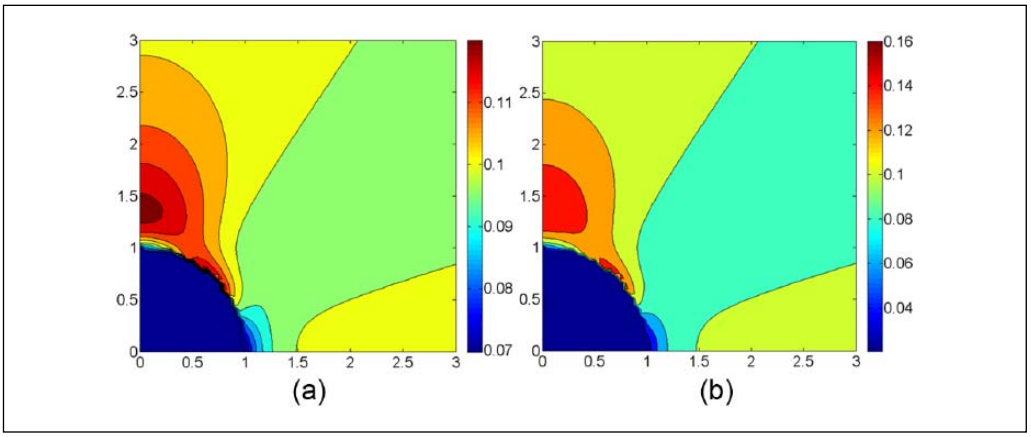


Figure 5: Strain fields in the numerical phantom containing a spherical inclusion embedded in the matrix under 0.1 remote strain: (a) MR = 2 and (b) MR = 10. MR = modulus ratio.

b) FEA Simulation

The results from Eshelby's solution were compared with those from FEA simulations using the same materials properties and boundary conditions. Axial stress and strain fields from FEA (Figure 6a and b) show excellent agreements with those from Eshelby's solution (Figure 4c and d). Results from FEA also confirm that the stress and strain levels inside the inclusion are almost uniform at 1.605 kPa and 0.0363, consistent with Eshelby's solution.

The variations of axial stress and strain from Eshelby's solution and FEA are plotted together along axial (z) and lateral (x) directions in Figure 6(c) and (d), respectively. It is notable that influences of the inclusion on both stress and strain persist much farther along axial direction than along lateral direction. Particularly the strain level converges on remote strain at a distance of about 1.5a (a: inclusion radius) in lateral direction, whereas it is still varying even at a distance of 3a in axial direction (Figure 6d).

In estimating the SR from elastogram, ideally matrix strain should be measured at an infinite distance from the inclusion. However, due to limited field of view of elastogram, measurements at the distance farther than twice the size of inclusion are usually unavailable. Among the three remote regions in the matrix (Figure 4d and b),

© 2019 Global Journals

the strain in the lateral region is relatively uniform (less than 3% deviation) and almost equal to remote strain (Figure 6d); thus, this region can be regarded as the best domain to measure the matrix strain. The strain plots in Figure 6(d) also indicate that the measurement should be made farther than a half-radius distance away from the inclusion to avoid the effect of inclusion.

c) MR versus SR—Spherical Inclusion

Results from Eshelby's solution and FEA clearly indicate that the stress inside the inclusion is more than 50% higher than the remote stress (1.605 kPa vs. 1 kPa in Figure 6c); furthermore, the strain is almost 80% higher than that directly obtained from Hooke's law (0.0366 vs. 0.02 in Figure 6d). As a result, SR value estimated from elastogram is much lower than the actual MR value (2.78 vs. 5.0). This type of discrepancy has been identified as the fundamental limitation of elastography[31]; thus, it was further investigated with Eshelby's solution to better understand the transfer characteristic of SR with respect to MR.

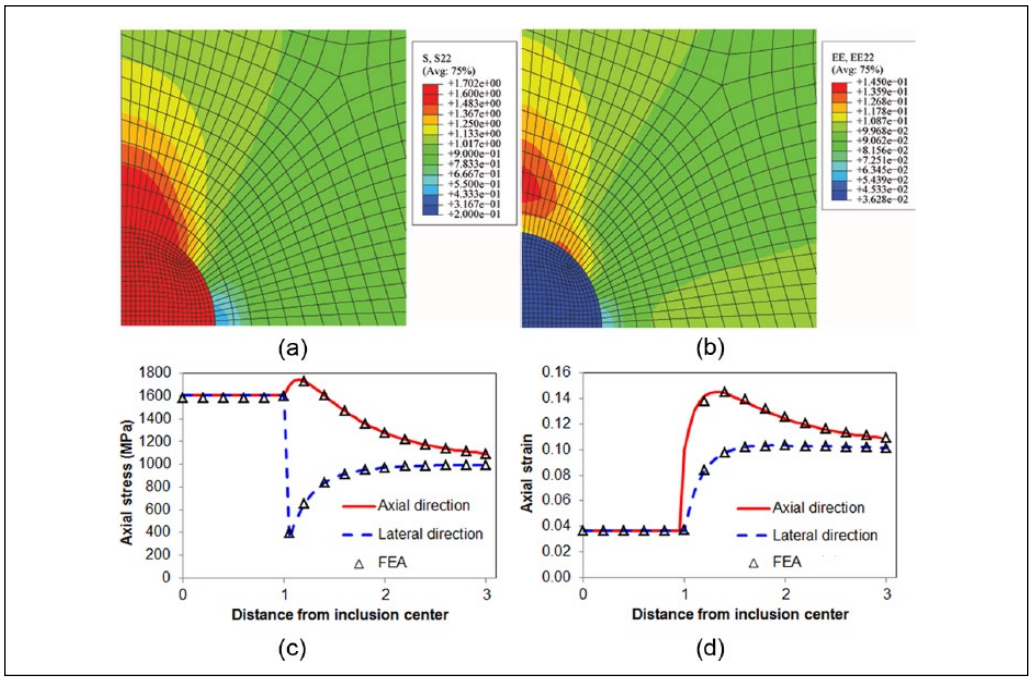


Figure 6: FEA simulation results: axial stress (a) and axial strain (b) distributions in the numerical phantom containing a spherical inclusion. The plots of axial stress (c) and axial strain (d) along axial (y) and lateral (x) directions from the inclusion center (inclusion radius = 1). Inclusion is five times stiffer than the matrix ($E^1/E^0 = 5$). Solid lines and triangles are predicted by Eshelby's solution and FEA, respectively. FEA = finite element analysis.

For the wide range of MR from −20 dB to 20 dB, SR was predicted with Eshelby's solution, as presented in Figure 7(a). It is notable that the SR curve is highly dependent on the MR that is proportional to inclusion modulus when matrix modulus is unchanged. For hard inclusions (MR > 0 dB), the curve follows the ideal curve with a relatively constant gap; however, for soft inclusions (MR < 0 dB), it shows significant deviation from the ideal curve.

Contrast-transfer efficiency (CTE) is sometimes expressed using the ratio of the observed contrast (SR) from the elastogram to the true contrast (MR) of the materials in decibels as[31]:

$$\eta(\mathrm{dB}) = |\mathrm{SR}(\mathrm{dB})| - |\mathrm{MR}(\mathrm{dB})|. \qquad (11)$$

CTE was predicted with Eshelby's solution, as plotted in Figure 7(b). CTE reaches the maximum when MR = 0 dB, that is, the inclusion and the matrix have the same modulus. The efficiency degrades rapidly as the inclusion becomes harder or softer.

In the medical practice using elastography, critical MR range for the diagnosis of the malignancy of the lesion is usually less than 2016; thus, the variation of SR for the MR range from 0.1 to 20 is plotted on a linear scale in Figure 7(c). The relationship between SR and MR is perfectly linear in this range, similar to the first-order relationship proposed by Kallel et al.14 SR (solid line) is less than a half of MR (dotted line) in most of the tested region, except for small MR (<1.28). The relationship is expressed as a first-order linear equation in Figure 7(c). Note that this relationship is valid only for spherical inclusion.

© 2019 Global Journals

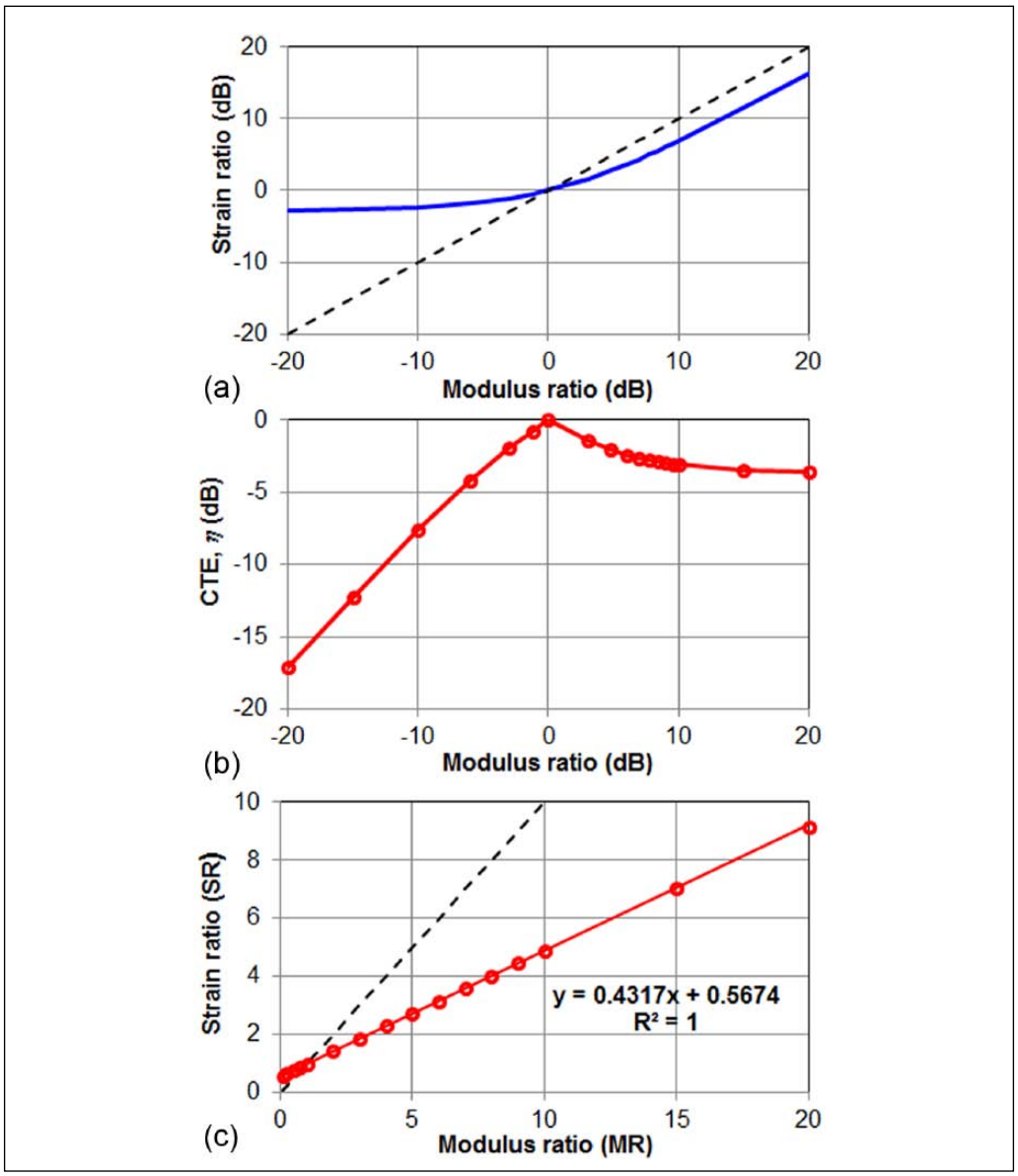


Figure 7: (a) Transfer characteristic curve of elastography predicted by Eshelby's solution (solid line) versus ideal curve (dotted line) on a log scale. (b) Contrast-transfer efficiency curve on a log scale. (c) SR versus MR on a linear scale. Dotted line is an ideal curve. SR = strain ratio; MR = modulus ratio.

d) Ellipsoidal Inclusion

It is known that benign and malignant lesions could differ significantly in shape. An adenoma (benign glandular lesion) has a more regular (close to spherical) shape whereas an adenocarcenoma (malignant glandular tumor) has an irregular or ellipsoidal shape.[17] The effect of ellipticity of an inclusion on SR was investigated by Eshelby's solution using the phantoms containing prolate (a = b = 0.2, c = 1, where a, b, and c are the x, y, and z axis, respectively; Figure 8a) and oblate (a = b = 1, c = 0.2; Figure 8c) spheroids. Although strain fields within the matrix can be divided into three regions and the strain level in each region is close to that around spherical inclusion (Figure 8b and d), the strains within the spheroidal inclusions are significantly different from those in the spherical inclusion. For example, the strain inside the prolate inclusion (0.0683 in Figure 8b) is much higher than that inside the oblate inclusion (0.0396 in Figure 8d). As a result, SR value varies significantly depending on the ellipticity of the inclusion.

© 2019 Global Journals

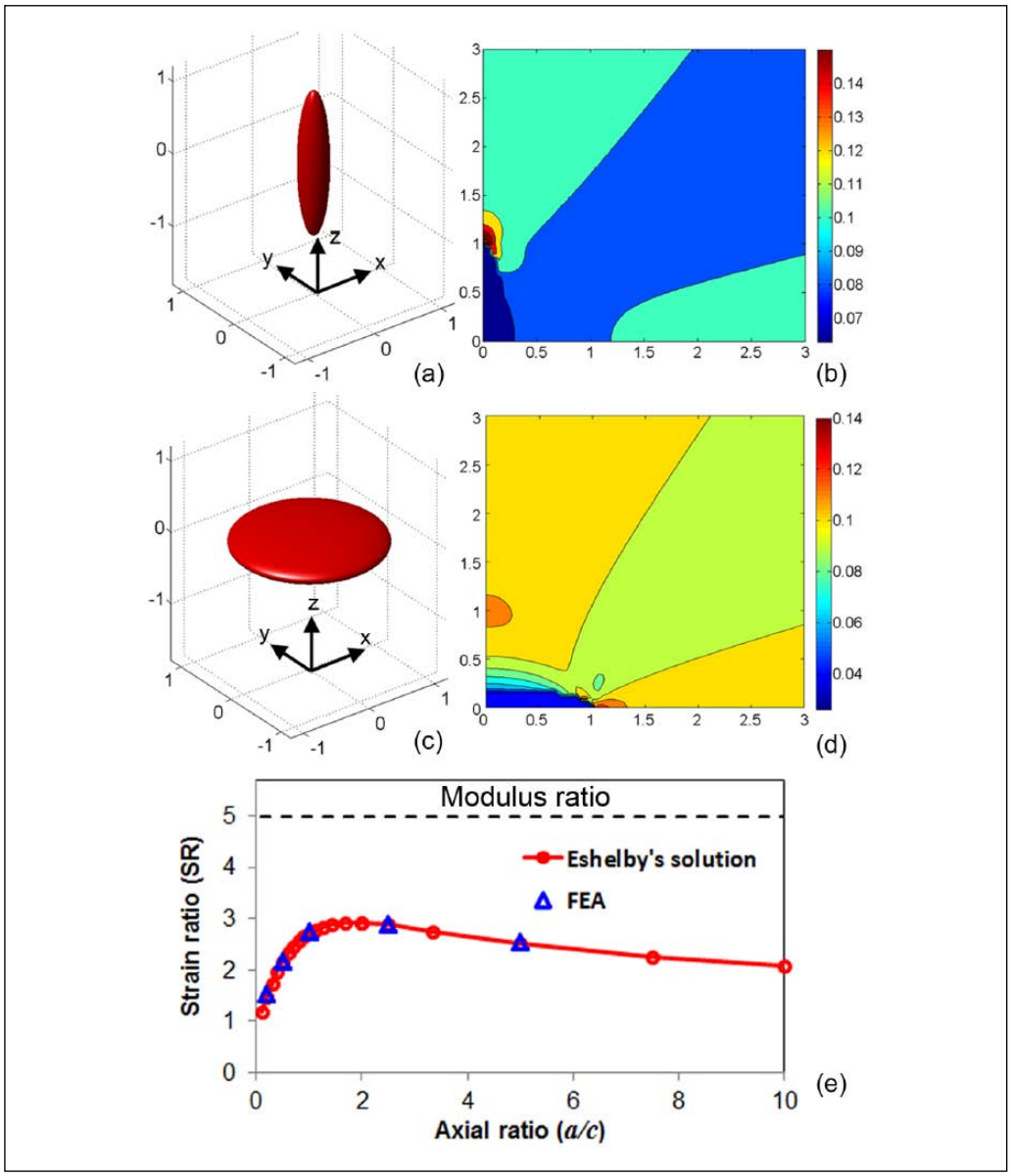


Figure 8: Elastic fields in the phantoms containing spheroidal inclusions: (a) a prolate inclusion (a = b = 0.2, c = 1), (b) the strain field around a prolate phantom, (c) an oblate inclusion (a = b = 1, c = 0.2), and (d) the strain field around an oblate inclusion. (e) Variation of SR (solid line) versus ideal curve (dotted line) against axial ratio (a/c). SR = strain ratio; FEA = finite element analysis.

Table 1: Strain Ratios for Various Axial Ratio and Modulus Ratios.

				a/c			
Modulus Ratio	0.5	1	1.333333	2	4	6.666667	10
1	1	1	1	1	1	1	1
2	1.548	1.392	1.358	1.34	1.386	1.456	1.514
4	2.132	1.74	1.66	1.632	1.768	1.976	2.18
6	2.442	1.896	1.794	1.764	1.956	2.268	2.592
8	2.632	1.984	1.872	1.84	2.072	2.456	2.872
10	2.76	2.04	1.92	1.89	2.15	2.58	3.07

The variation of SR with respect to the axial ratio (a/c) is predicted by Eshelby's solution and plotted (circle) in Figure 8(e). For verification purpose, some data points were also determined by FEA and plotted on the same graph (triangle). Figure 8(e) indicates that SR reaches the maxi- mum (2.92) when a/c is 2, and decreases with the change of a/c in both directions, more rapidly in prolate direction. Note that the maximum SR value of 2.92 is still much lower than the actual MR (5.0, dotted horizontal line).

© 2019 Global Journals

e) Surface Regression Model

SRs for various combinations of a/c and MR are summarized in Table 1. Because SR varies non- linearly against a/c, linear regression models such as Equation (1)[14] or Equation (2)[33] cannot be adopted for ellipsoidal inclusions. Instead, we considered a surface regression model with two predictor data (SR and a/c) and one response data (MR). This was achieved by applying a surface-fitting tool in Matlab (R2012b), cftool, to the data in Table 1. Using a polynomial regression model, MR could be formulated as a coupled polynomial equation of the order 4 × 2 as follows:

$$MR = p00 + p10\,x + p01\,y + p20\,x^2 + p11\,xy + p02\,y^2 + p30\,x^3 + p21\,x^2y + p12\,xy^2 + p40\,x^4 + p31\,x^3y + p22\,x^2y^2. \quad (12)$$

where x = a/c, y = SR, and the coefficients are listed in Table 2. Good agreement was obtained between the model and the data in Table 1 ($R^2 = 0.992$). Figure 9(a) shows the fitted surface from the model to the data in 3D and Figure 9(b) illustrates the 2D contour plot of the same surface.

f) Gelatin-Based Phantoms

The polynomial function in Equation (12) was applied to gelatin phantoms containing a spherical inclusion. MR was estimated first by performing the compression tests on 20% (inclusion) and 5% (matrix) gelatin cylindrical samples. Representative engineering stress–strain curves from the compression tests are shown in Figure 10. Loading curves were regarded as linear with R^2 value 0.9971 and 0.9849, for 20% and 5% gelatin content samples, respectively. Loading modulus was determined to be 51 ± 2 kPa and 10 ± 1 kPa for each content, respectively.

Table 2: Coefficients of Polynomial Regression Function in Equation (12).

p^{00}	p^{10}	p^{01}	p^{20}	p^{11}	p^{02}
−2.439	−0.4783	4.827	0.747	−1.887	−0.2935
p^{30}	p^{21}	p^{12}	p^{40}	p^{31}	p^{22}
−0.1538	0.3153	0.166	0.00832	−0.0136	−0.0135

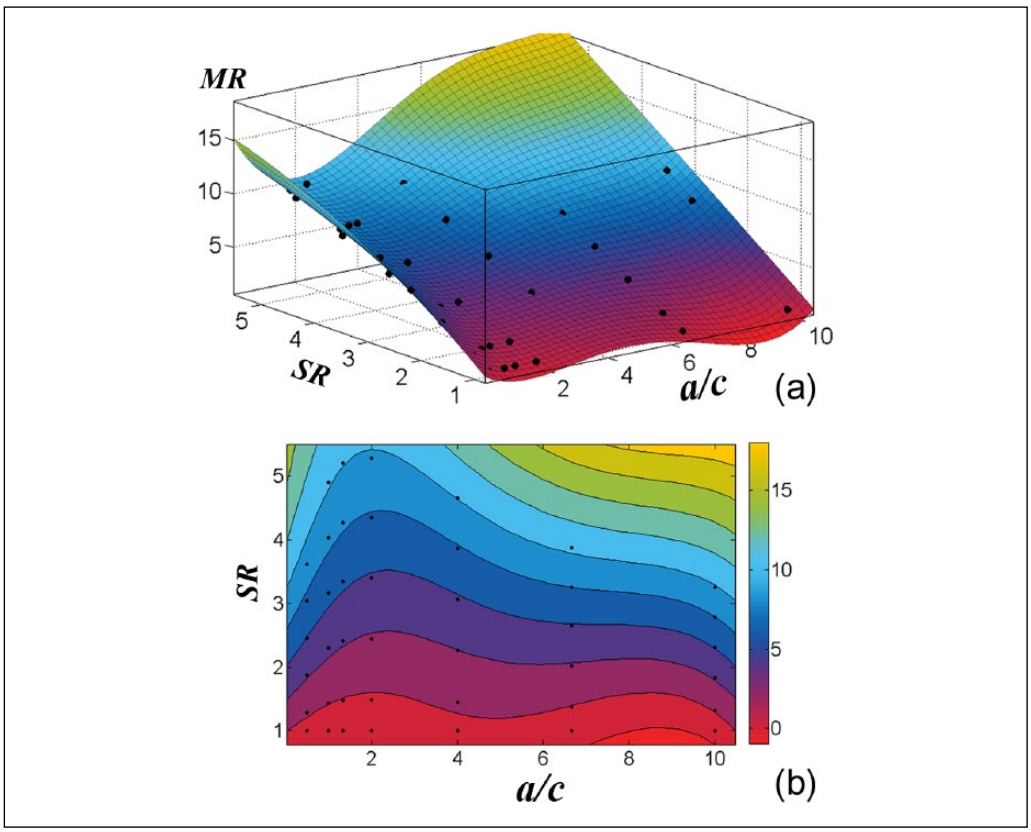


Figure 9: Surface fitting of a 4 × 2 polynomial function to the data in Table 1: (a) 3D surface plot, and (b) 2D contour plot. MR = modulus ratio; SR = strain ratio.

© 2019 Global Journals

To estimate the SR, gelatin phantoms were US imaged from the side while compressive loading was applied to the top (arrows in Figure 11a) and the DGE elastograms were generated from the US images. Figure 11(b) is the elastogram of a phantom compressed at 10% strain. Consistent with Eshelby's solution, strain field within the inclusion is almost uniform at 0.036, while the strain significantly varies in the matrix. As discussed in the previous section, the measurement of matrix strain should be made in the lateral region (circled region A) which is distant from the inclusion center by more than 1.5 times of the inclusion radius in the lateral direction. Region B is also a candidate, but the region closer to the probe is generally preferable. Measured strain is 0.1 at A; thus, SR is calculated to be 2.78. By substituting the SR into Equation (12), MR is estimated to be 5.60. These results are close to the predictions from Eshelby's solution (SR = 2.73) and actual MR (5.1).

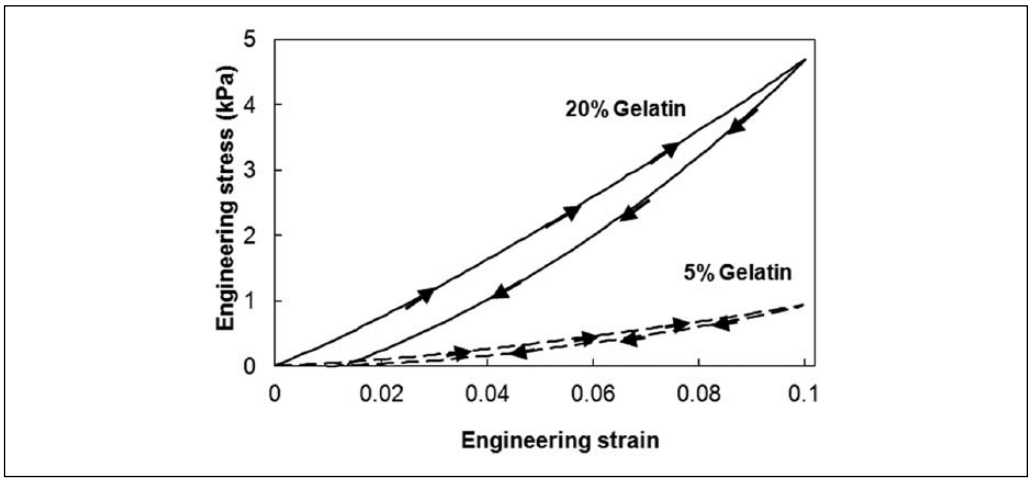


Figure 10: Engineering stress–strain curves for 20% (solid line) and 5% (dotted) gelatin samples from simple compression tests.

Figure 11(c) is the elastogram of a phantom where a part of the inclusion is dissolved into the matrix, mimicking a carcinoma infiltrating into the surrounding tissue. In this image, the strain in the right side of the inclusion cannot be measured due to the infiltrated domain, thus the strain in the left side of inclusion (circled region) is measured as a matrix strain (0.11). The strain level inside the inclusion is 0.035 and the SR is calculated to be 3.05, which are slightly higher than that of spherical inclusion. Assuming the axial ratio of 1.5, MR is estimated to be 5.46 that are consistent with the actual MR value.

Strain field in the matrix can be distorted or localized due to inhomogeneous lesions or local loadings. Figure 11(d) shows highly concentrated compressive deformation above the inclusion, which is caused by the locally concentrated loading on top of the phantom. Although strain field varies significantly along the loading direction, strain along the lateral direction is relatively consistent, and the measured strain value is almost the same as the applied strain (0.1). Inclusion strain is also uniform at 0.035, thus the SR (2.86) is almost the same as the other cases, and the MR is estimated to be 5.8 for circular inclusion.

The above results indicate that elastic fields in the elastograms of gelatin-based phantoms are well predicted by Eshelby's solution. Furthermore, the surface regression model proposed in Equation (12) can successfully predict the actual MRs of gelatin phantoms. Therefore, the pro- posed method has the potential to improve the diagnostic performance of elastography in breast cancer screening practice, as described in the subsequent sections.

g) Clinical Applications

Human breasts are made up of fatty tissue with epithelial and stromal tissues and a number of masses inside, each of which has different echographic properties. Naturally, US and elastogram images commonly contain complex and noisy patterns, which require particular attention for the understanding and the utilization of them. This is particularly true for BIRADS 3 and 4 lesions that are occasionally misdiagnosed even by experienced radiologists. Several case studies are presented here for the lesions in different BIRADS categories.

© 2019 Global Journals

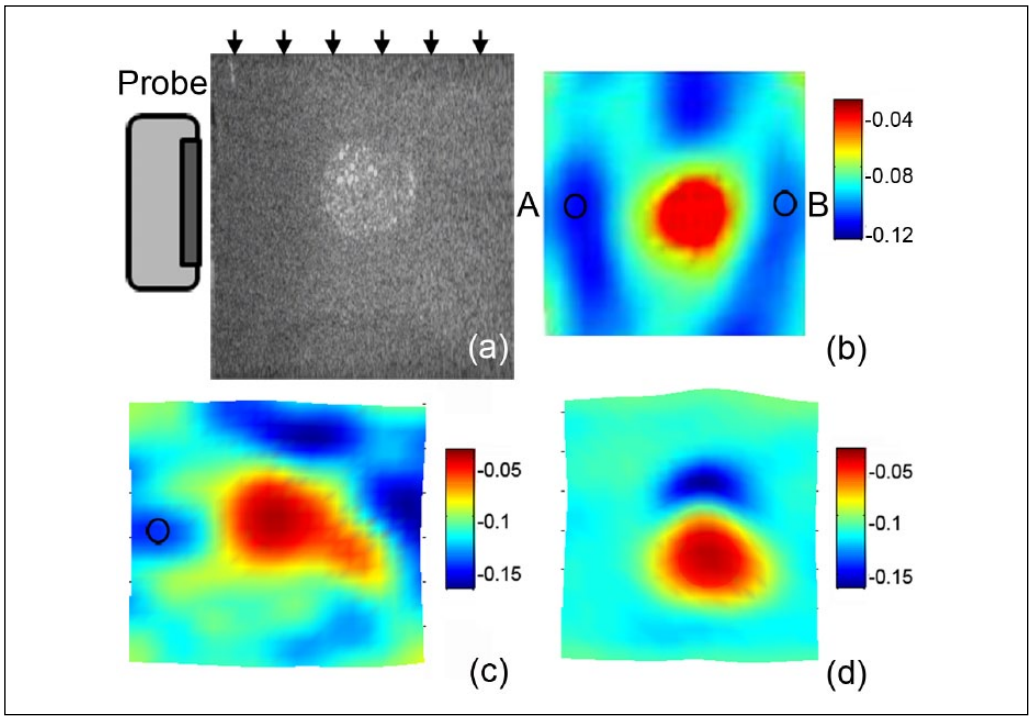


Figure 11: (a) US image of a gelatin phantom containing a stiff inclusion (E^1/E^0 = 5.1). Elastograms of gelatin phantoms with; (b) circular inclusion compressed up to 10% strain; (c) partially dissolved inclusion mimicking infiltrating carcinoma; (d) locally deformed matrix.

Case 1: BIRADS 4 Lesion—Malignant

Figure 12(a) are the US image of a BIRADS 4 lesion where compressive load was applied to the top side of the image, and the elastogram produced from the dotted rectangular region in the US image. The elastogram shows that there is a stiff oblate lesion in the center deformed at about −0.008 strain. Matrix strain is hard to be estimated, as the lateral strains are not consistent along lateral direction, that is, the strain in the right side of the inclusion is much higher (−0.06) than that in the left side (−0.042). However, another stiff lesion can be seen in the right-bottom corner, and the tissue between two stiff lesions might be under higher local deformation. Therefore, the strain in the left side of the inclusion is regarded as the matrix strain, and the SR is estimated to be 5.25. Taking the a/c of 2.5, MR is estimated to 9.79 from Equation (12). As the estimated MR is in the range of cancerous lesions,[16] this lesion is deemed malignant. Biopsy confirmed that it is an invasive mammary carcinoma.

Case 2: BIRADS 4 Lesion—Malignant

Figure 12(b) is the US image and the elastogram of a BIRADS 4 lesion. The shape of the lesion is not identifiable on the US image, but the elastogram clearly shows the existence of a large stiff lesion in the middle of the image. Highly compressed tissue is also observed above the lesion. The inclusion strain is about −0.01, whereas the matrix strain is about −0.05 in the left and −0.03 in the right sides of the lesion, respectively. As the lesion looks connected further to the right-side direction in the US image, the strain in the left side (−0.05) is taken as a matrix strain. By substituting the a/c of 1.6 and SR of 5, MR is estimated to be 9.37. Because this value is higher than the reported MR for cancer (∼7),[17] this lesion is diagnosed as a malignant tumor. Biopsy indicated that this is an invasive ductal carcinoma.

Case 3: BIRADS 4 Lesion—Benign

The lesion in Figure 12(c) is highly noticeable in US image and was classified as a BIRADS 4 lesion by a radiologist, which is usually regarded as malignant. In the elastogram, it shows a diagonally spread shape over a wide area, and is regarded as an oblate ellipsoid with the a/c of 2.2. Inclusion strain is not uniform, ranging from −0.052 to −0.03, whereas tissue strain is at about −0.05. Therefore, the maximum SR is up to 2.5 and the corresponding MR is estimated to be 3.86 from Equation (12). As this value is much lower than the reported range of MR for cancer, it may not be malignant. According to biopsy result, this is a benign fibroadenoma. A small lower strain region can be found in the left bottom corner. Although not histologically examined, this region may be another lesion.

© 2019 Global Journals

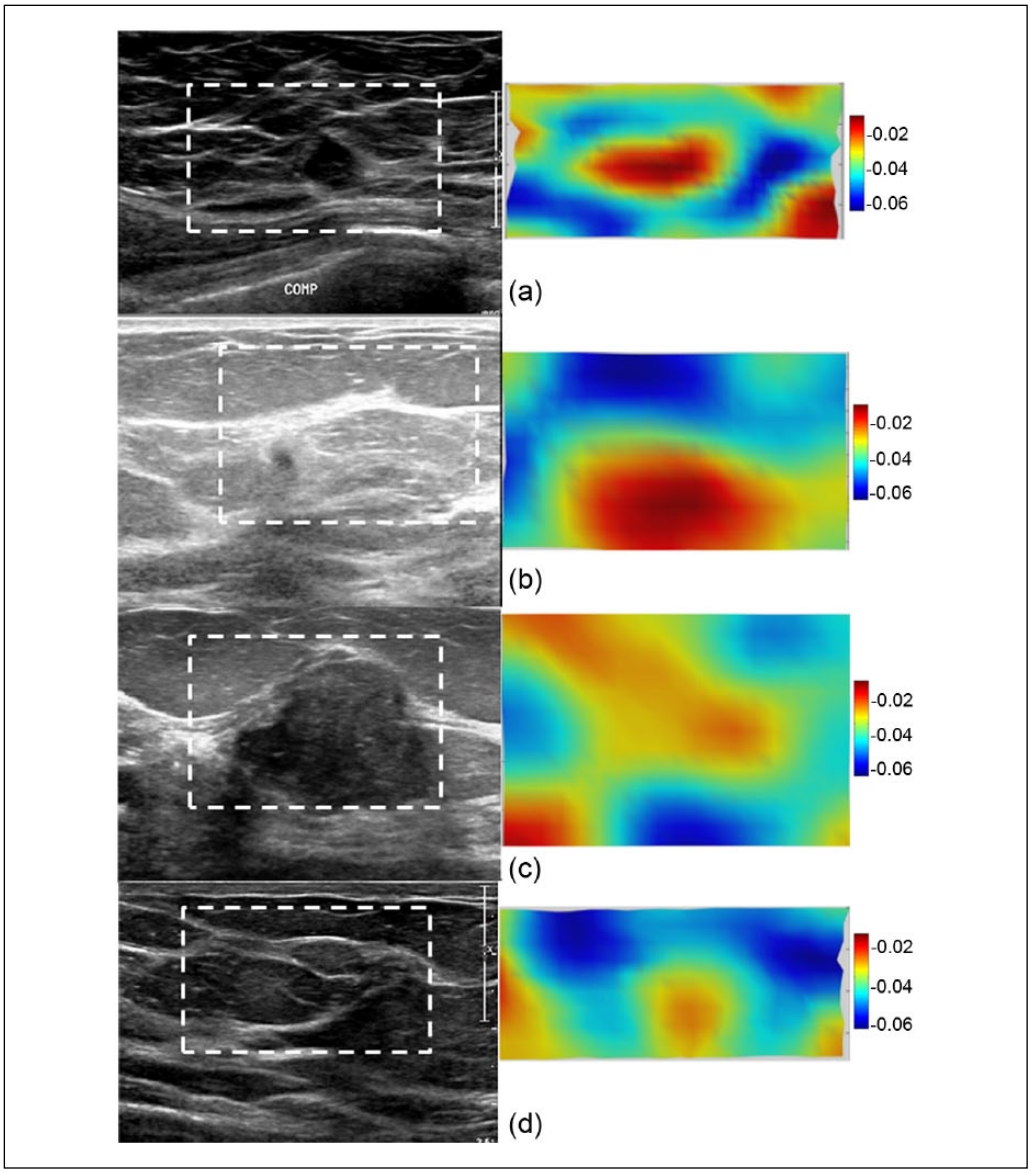


Figure 12: US images and elastograms of human breasts containing: (a) an invasive mammary carcinoma (BIRADS 4); (b) an invasive ductal carcinoma (BIRADS 4); (c) a fibroadenoma (BIRADS 4); (d) a necrotic hemorrhage (BIRADS 5).

Case 4: BIRADS 5 Lesion—Benign

The lesion in Figure 12(d) was clearly visible in the US image and was classified as BIRADS 5 by a radiologist. In the elastogram, inclusion strain is −0.025, while the matrix strain is between −0.05 and −0.055. Assuming a circular inclusion and adopting the higher SR of 2.2 for sensitivity, the MR is estimated to be 4.13. Usually BIRADS 5 lesion is regarded as highly likely malignant; however, the low MR value suggests that this lesion should not be malignant. Biopsy confirmed that this lesion is a benign fibrosis with a necrotic hemorrhage.

IV. Data Analysis and Discussion

Among the 44 lesions examined, biopsy results indicated that 21 were benign and 23 were malignant, as summarized in Table 3. The most common malignant tumors were invasive mammary carcinoma and invasive ductal carcinoma (n = 9 for both), and the most common benign tumor was fibroadenoma (n = 7). As shown in Figure 13, the mean SR of malignant tumors was 6.26 ± 2.06, and that for benign entities was 1.39 ± 0.80. However, the mean MR of malignant tumors and benign lesions was 12.71 ± 4.33 and 1.88 ± 1.82, respectively.

The significances of the differences in SR and MR were tested by applying Tukey's post hoc test using q score determined by the following formula:

$$q = \frac{M_1 - M_2}{\sqrt{\frac{MS_w}{n}}}, \tag{13}$$

© 2019 Global Journals

where M_1 and M_2 are the mean value of each group, MSw is mean square within, and n is the number per each group. The relevant variables are listed in Table 4. From the Tukey's significance/probability table,[47] critical Tukey's score (qcrit) corresponding to 95% confidence is 2.86. The q score determined for SR and MR are 14.01 and 15.39, respectively, thus it can be concluded that unequal variances exist within the groups, and the differences are significant.

This can be further verified with unpaired two-sample t test.[48] For SR, t statistic is calculated to be 2.35. For the degree of freedom (df) of 43, t value for 95% confidence level was 2.0181; thus the SRs between malignant tumors and benign lesion were significantly different ($p < 0.05$) with a small margin. However, t statistic for MR was 11.09; thus, the difference of MRs between malignant tumors and benign entities were statistically significant with a much higher confidence level ($p < 0.00001$).

Using the receiver-operating characteristic (ROC) curve of SR, the area under the curve (AUC) was 0.9341, and the best cutoff SR value of 3.1 was obtained at the maximum Youden's index of 0.86957. With this cutoff SR, the sensitivity, specificity, and accuracy were 91.3%, 90.5%, and 90.9%, respectively. For ROC curve of MR, AUC was 0.94824, and the best cutoff MR was 5.67 at the maximum Youden's index of 0.95238. The sensitivity, specificity, and accuracy were 100%, 95.2%, and 97.7%, respectively.

Table 3: Histologic Diagnoses in 44 Patients with Benign or Malignant Breast Lesions.

Benign Lesions (21)		Malignant Lesions (23)	
Diagnosis	n	Diagnosis	n
Fibroadenoma	7	Mammary carcinoma (invasive, infiltrating)	9
Cyst	5		
Fibrocyst	1	Ductal carcinoma (invasive, infiltrating)	9
Fibro fatty tissue	2		
Fibrosis	1	Ductal carcinoma in situ (DCIS)	3
Benign fibro-epithelial tissue	2	Neuroendocrine carcinoma	1
Benign lactating adenoma	1	Metaplastic carcinoma	1
Other benign tissue	2		

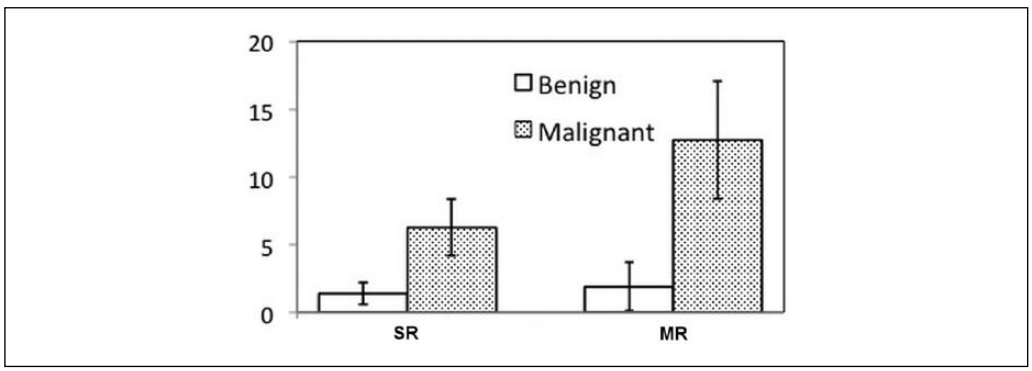


Figure 13: Mean values of SR and MR for benign and malignant cases, respectively. SR = strain ratio; MR = modulus ratio.

Table 4: Relevant Variables for Tukey's Post Hoc Test.

Variables	SR		MR
M_1 (Mean, Malignant) M_2 (Mean, Benign) n (Number of samples)	6.261 ± 2.063 1.390 ± 0.804 21		12.712 ± 4.329 1.882 ± 1.817 23
k (Number of groups)		2	
df Among groups		1	
df Within groups		42	
SS_{within} (Sum of squares within groups)	106.566		478.341
MS_{within} (Mean squares within groups)	2.537		11.389
q (Tukey's score)	14.014		15.389
q_{crit} (Critical q score, 95% confidence)		2.86	

SR = strain ratio; MR = modulus ratio.

© 2019 Global Journals

The proposed surface regression model considers only two input parameters, a/c and SR, to predict MR. Nevertheless the adoption of MR in breast cancer screening could significantly improve both confidence level and the diagnostic performance, compared with SR. In statistical analysis, the mean of SR was different by 4.87 between benign and malignant lesions, whereas the difference of the mean of MR increased up to 10.83. Considering the standard deviation (2.06 and 0.80 for SR and 4.33 and 1.82 for MR), the difference between benign and malignant SR can be even smaller, increasing the ratio of gray cases that require further invasive testing. However, the means of MR for benign and malignant lesions are different enough to differentiate between benign and malignant lesions, thus benign biopsy could be reduced by using MR.

The proposed approach has an artifact that a/c ratio can be varied depending on the application angle of US probe, but by manipulating the probe angle with imaging the lesion, maximum a/c for oblate lesion or minimum a/c for prolate lesion can be obtained for conservative assessment of MR. Also, the proposed approach is still limited to relatively simple ellipsoidal shapes and the protocols for irregular shapes of lesion have been yet established, which may be the next milestone of the future research.

V. Conclusion

We investigated the transfer characteristic of observed contrast, SR, from elastography in predicting the true contrast, MR, by using the Eshelby's solution. It was found that SR not only significantly underestimates MR, but also varies with the shape and the modulus of the lesion. A surface regression model to predict MR from axial ratio and SR was proposed and verified through the application to gelatin phantoms. The model was further applied to human breast elastograms containing different types of lesions, and statistical analysis indicated that significant improvement in both confidence level and diagnostic performance could be achieved by adopting MR predicted by the model. The model can be utilized for the screening of breast cancer by comparing the correlated MR from elastography with actual modulus data of various tissues from mechanical testing.

Appendix

Supplementary Materials

Matlab codes for Eshelby's solution associated with this article can be found in the online version. Please run Eshelby_GUI.m, which can be found from Eshelby.rar.

Declaration of Conflicting Interests

The author(s) declared no potential conflicts of interest with respect to the research, authorship, and/or publication of this article.

Funding

The author(s) disclosed receipt of the following financial support for the research, authorship, and/or publication of this article: The work was supported by Natural Sciences and Engineering Research Council of Canada (NSERC). Clinical trial was approved by Tri-Hospital Research Ethics Board (THREB#2013-0508: Application of Displacement-Gradient Elastography to the Diagnosis of Breast Cancer). All clinical data were provided by Grand River Hospital, Kitchener, Ontario, Canada.

References Références Referencias

1. Siegel R, Naishadham D, Jemal A. Cancer statistics, 2013. C A Cancer J Clinic. 2014; 63: 11-30.
2. Levy L, Suissa M, Chiche J F, Teman G, Martin B. BIRADS ultrasonography. Eur J Radiol. 2007; 61: 202-11.
3. Smith R A, Cokkinides V, Eyre H J. American Cancer Society guidelines for the early detection of cancer. CA Cancer J Clinic. 2006; 56: 11-25.
4. Ophir J, Alam S K, Garra B S, Kallel F, Konofagou E E, Krouskop T, et al. Elastography: imaging the elastic properties of soft tissues with ultrasound. J Med Ultrason. 2002; 29: 155-71.
5. Skovoroda A R, Klishko A N, Gusakyan D A, Mayevskii Y I, Yermilova V D, Oranskaya G A, et al. Quantitative analysis of the mechanical characteristics of pathologically changed soft biological tissues. Biophysics. 1995; 40: 1359-64.
6. Ophir J, Cespedes I, Garra B, Ponnekanti H, Huang Y, Maklad N. Elastography: ultrasonic imaging of tissue strain and elastic modulus in vivo. Eur J Ultrasound. 1996; 3: 49-70.
7. Kwon H J, Lee J. Low-cost quasi-real-time elastography using B-mode ultrasound images. Biomed Mater Eng. 2014; 24: 1673-92.
8. Bercoff J, Tanter M, Fink M. Supersonic shear imaging: a new technique for soft tissue elasticity mapping. IEEE Trans Ultrason Ferroelectr Freq Control. 2004; 51: 396-409.
9. Fink M, Tanter M. Multiwave imaging and super resolution. Phys Today. 2010; 63: 28-33.
10. Tanter M, Bercoff J, Athanasiou A, Deffieux T, Gennisson J-L, Montaldo G, et al. Quantitative assessment of breast lesion viscoelasticity: initial clinical results using supersonic shear imaging. Ultrasound Med Biol. 2008; 34: 1373-86.
11. Itoh A, Ueno E, Tohno E, Kamma H, Takahashi H, Shiina T, Yamakawa M, et al. Breast disease: clinical application of US elastography for diagnosis. Radiol. 2006; 239: 341-50.
12. Thomas A, Degenhardt F, Farrokh A, Wojcinski S, Slowinski T, Fisher T. Significant differentiation of focal breast lesions: calculation of strain ratio in breast sonoelastography. Acad Radiol. 2010; 17: 558-63.

© 2019 Global Journals

13. Zhi H, Xiao X Y, Yang H Y, Ou B, Wen Y L, Luo B M. Ultrasonic elastography in breast cancer diagnosis: strain ratio vs 5-point scale. Acad Radiol. 2010; 17: 1227-33.
14. Kallel F, Bertrand M, Ophir J. Fundamental limitations on the contrast-transfer efficiency in elastography: an analytic study. Ultrasound Med Biol. 1996; 22: 463-70.
15. Celi S, Di Puccio F, Forte P. Advances in finite element simulations of elastosonography for breast lesion detection. J Biomech Eng. 2011; 133: 081006.
16. Krouskop T A, Wheeler T, Kallel F, Garra B. Elastic moduli of breast and prostate tissues under compression. Ultrason Imaging. 1998; 35: 260-74.
17. Sarvazyanm A P, Skovoroda A R, Emelianov S Y, Fowlkes J B, Pipe J G, Adler R S, et al. Biophysical bases of elasticity imaging. Acoust Imag. 1995; 21: 223-40.
18. Samani A, Zubovits J, Plewes D. Elastic moduli of normal and pathological human breast tissues: an inversion-technique-based investigation of 169 samples. Phys Med Biol. 2007; 52: 1565-76.
19. Raghavan K R, Yagle A E. Forward and inverse problems in elasticity imaging of soft-tissues. IEEE Trans Nucl Sci. 1994; 41: 1639-48.
20. Skovoroda A R, Aglyamov S R. Reconstruction of elastic properties of soft biological tissues exposed to low-frequencies disruption. Biofizika. 1995; 40: 1329-34.
21. Sumi C, Suzuki A, Nakayama K. Phantom experiment on estimation of shear modulus distribution in soft-tissue from ultrasonic measurement of displacement vector field. IEICE Trans Fundam Electron Commun Comput Sci. 1995; 78: 1655-64.
22. Sumi C. Spatially variant regularization for tissue strain measurement and shear modulus reconstruction. J Med Ultrasonics. 2007; 34: 125-31.
23. Le Floc'h S, Cloutier G, Finet G, Tracqui P, Pettigrew RI, Ohayon J. Vascular imaging modulography: an experimental in vitro study. Comput Methods Biomech Biomed Eng. 2010; 13: 89-90.
24. Barbone P E, Oberai A A. Elastic modulus imaging: some exact solutions of the compressible elastography inverse problem. Phys Med Biol. 2007; 52: 1577-93.
25. Kallel F, Bertrand M. Tissue elasticity reconstruction using linear perturbation method. IEEE Trans Med Imaging. 1996; 15: 299-313.
26. Richards M S, Barbone P E, Oberai A A. Quantitative three-dimensional elasticity imaging from quasi- static deformation: a phantom study. Phys Med Biol. 2009; 54: 757-79.
27. Jiang J, Varghese T, Brace C L, Madsen E L, Hall T J, Bharat S, et al. Young's modulus reconstruction for radio-frequency ablation electrode-induced displacement fields: a feasibility study. IEEE Trans Med Imaging. 2009; 28: 1325-34.
28. Baldewsing R A, Schaar J A, Mastik F, Oomens CWJ, van der Steen AFW. Assessment of vulnerable plaque composition by matching the deformation of a parametric plaque model to measured plaque deformation. IEEE Trans Med Imaging. 2005; 24: 514-28.
29. Oberai A A, Gokhale N H, Feijoo G R. Solution of inverse problems in elasticity imaging using the adjoint method. Inverse Probl. 2003; 19: 297-313.
30. Samani A, Bishop J, Plewes D B. A constrained modulus reconstruction technique for breast cancer assessment. IEEE Trans Med Imaging. 2001; 35: 877-85.
31. Ponnekanti H, Ophir J, Huang Y, Cespedes I. Fundamental mechanical limitations on the visualization of elasticity contrast in elastography. Ultrasound Med Biol. 1995; 21: 533-43.
32. Baldewsing R A, Mastik F, Schaar J A, Serruys P W, van der Steen AFW. Young's modulus reconstruction of vulnerable atherosclerotic plaque components using deformable curves. Ultrasound Med Biol. 2006; I3 (2): 201-10.
33. Bilgen M, Insana M. Elastostatics of a spherical inclusion in homogeneous biological media. Phys Med Biol. 1998; 43: 1-20.
34. Alberts B, Bray D, Lewis J, Raff M, Roberts K, Watson J D. Molecular Biology of the Cell. 3rd ed. New York and London: Garland Publishing; 1994; pp. 1255-8.
35. Fung YCB. Elasticity of soft tissues in simple elongation. Am J Physiol. 1967; 213: 1532-44.
36. Doyley M M. Model-based elastography: a survey of approaches to the inverse elasticity problem. Phys Med Biol. 2012; 57: R35-73.
37. Eshelby J D. The determination of the elastic field of an ellipsoidal inclusion. Proc R Soc Lond. 1957; A241: 376-92.
38. Eshelby J D. The elastic field outside an ellipsoidal inclusion, and related problems. Proc R Soc Lond. 1959; A252: 561-9.
39. Ju J W, Sun L Z. A novel formulation for the exterior-point Eshelby's tensor of an ellipsoidal inclusion. J Appl Mech. 1999; 66: 570-4.
40. Mura T. Micromechanics of Defects in Solids. Dordrecht: Kluwer Academic; 1987.
41. Ju J W, Sun L Z. Effective elastoplastic behaviour of metal matrix composites containing randomly located aligned spheroidal inhomogeneities. Part I: micromechanics-based formulation. Int J Solid Struct. 2001; 38: 183-201.
42. Han Y, Kim D W, Kwon H J. Application of digital image cross-correlation and smoothing function to the diagnosis of breast cancer. J Mech Behav Biomed Mater. 2012; 14: 7-18.

© 2019 Global Journals

43. Han Y, Rogalsky A D, Zhao B, Kwon H J. The application of digital image techniques to determine the large stress - strain behaviors of soft materials. Polym Eng Sci. 2011; 52: 826-34.
44. Pavan T Z, Madsen E L, Frank G R, Jiang J, Carneiro AAO, Hall T J. A nonlinear elasticity phantom containing spherical inclusions. Phys Med Biol. 2012; 57: 4787-804.
45. Wahba G. Spline Models for Observational Data, volume 59 of Series in Applied Mathematics. Philadelphia, PA: SIAM; 1990; pp. 45-65.
46. Madsen E L, Zagzebski J A, Frank G R. An anthropomorphic ultrasound breast phantom containing intermediate-sized scatterers. Ultrasound Med Biol. 1982; 8: 381-92.
47. Champion D F, Hartley R D. Statistics for Criminal Justice and Criminology. 3rd ed. Boston, MA: Prentice Hall; 2009.
48. Mould R F. Introductory Medical Statistics. 3rd ed. Bristol, UK: IOP Publishing Ltd; 1998.

© 2019 Global Journals